Pressure-induced topological and structural phase transitions in natural van der Waals heterostructures from the $(SnTe)_m(Bi_2Te_3)_n$ homologous family: Raman spectroscopy, x-ray diffraction, and density functional theory

Sukanya Pal,[1,*] Raagya Arora,[2,*] Ananya Banik,[3] K. V. Glazyrin,[4] D. V. S. Muthu,[1] Kanishka Biswas,[5] U. V. Waghmare,[2] and A. K. Sood[1,†]

[1]*Department of Physics, Indian Institute of Science, Bangalore 560012, India*
[2]*Theoretical Sciences Unit, Jawaharlal Nehru Center for Advanced Scientific Research, Jakkur P.O., Bangalore 560064, India*
[3]*Institute of Inorganic and Analytical Chemistry, University of Münster, Corrensstrasse 30, 48149 Münster, Germany*
[4]*Photon Sciences, Deutsches Elektronen Synchrotron, D-22607 Hamburg, Germany*
[5]*New Chemistry Unit, Jawaharlal Nehru Center for Advanced Scientific Research, Jakkur P.O., Bangalore 560064, India*

(Received 6 January 2022; accepted 28 September 2022; published 13 October 2022)

A new class of van der Waals heterostructures of $(SnTe)_m(Bi_2Te_3)_n$ (with $m = 1, 2, ..$ and $n = 1, 2, ..$), consisting of a topological crystalline insulator SnTe and a topological insulator Bi_2Te_3 are emerging with exciting properties and applications, such as in thermoelectrics. Our study examines the stability of these heterostructures ($m = 1$ and $n = 1,2$) under pressure using Raman scattering, synchrotron x-ray diffraction, and density functional theory. Raman studies as a function of pressure carried out at room temperature reveal a phase transition in the pressure regime of 3–5 GPa for both the compounds, which is shown to be associated with an electronic topological transition involving change in the Z_2 topological invariant. In addition to the electronic changes, our Raman experiments indicate that rhombohedral ($R\bar{3}m$) $SnBi_2Te_4$ undergoes structural transition at ∼6.0 to a possible monoclinic phase and another transition at ∼12.0 GPa. Raman and x-ray diffraction experiments on trigonal ($P\bar{3}m1$) $SnBi_4Te_7$ show two structural transitions at ∼9.5 GPa to a monoclinic phase followed by one to cubic phase at ∼14.1 GPa. Our analysis of electronic structure reveals that the phase transition at 9.5 GPa in $SnBi_4Te_7$ is accompanied by an insulator to semimetal transition.

DOI: 10.1103/PhysRevB.106.134104

I. INTRODUCTION

In recent years, many new materials have been discovered with exotic electronic properties, of which topological insulators (TIs) have attracted a lot of attention. Three-dimensional (3D) Z_2 TIs are characterized by spin-polarized surface states in the bulk energy gap arising from inverted band gap at an odd number of symmetry points of the bulk Brillouin zone [1,2]. Spin-orbit coupling plays a crucial role in causing band inversions and these surface states are protected from backscattering of carriers in the presence of weak perturbations, by time-reversal symmetry [3,4]. Bi_2Te_3 is a material that belongs to the family of 3D TIs [5,6]. On the other hand, topological crystalline insulators (TCI) are a class of 3D TIs with some distinct features. TCIs are also characterized by spin-polarized, linearly dispersive surface states similar to a 3D TI, however, the major difference is that, crystal symmetries give rise to the topological nature of the electronic structures [7]. A TCI is not a Z_2 TI because an even number of band inversions, which give rise to a nonzero mirror Chern number, characterizes a TCI. In addition, the crystalline symmetry plays a major role in protecting the surface states [8,9]. SnTe is an example of a TCI at ambient condition [10,11] and undergoes a TCI to normal semiconductor transition at ∼5.8 GPa [12]. Bi_2Te_3 undergoes an electronic topological transition [13,14] as a function of pressure. Search for new TIs continues, and in recent years, heterostructure engineering has been attracting attention, owing to its ability to alter stacking sequence of layers of different materials and insertion of different building blocks into the crystal giving rise to robust nontrivial topological properties.

Many 2D materials with stable nanosheets have stimulated activity to design and predict new materials with van der Waals heterostructures. Various studies have been performed to design new TIs with pseudobinary systems like $nA^{IV}B^{VI} - mA_2{}^{V}B_3{}^{VI}$ (A^{IV} = Ge, Sn, Pb; A^{V} = Bi, Sb; B^{VI} = Te, Se) [15–17]. Exotic topological and thermoelectric properties of single/few-layer Bi_2Te_3 have stimulated interest in studying the layered complex structural compounds of the $(A^{IV}Te)_n(Bi_2Te_3)_m$ pseudobinary homologous series. These materials have complex unit cells, which consist of covalently bonded $Te_2 - Bi - Te_1 - A^{IV} - Te_1 - Bi - Te_2$ blocks stacked along the c axis which are connected by van der Waals interaction (n=m=1) or separated by Bi_2Te_3 interlayers ($m > n$). Compounds having the same A^{IV} element belong to a homologous series with similar a and b lattice parameters but different c parameter depending on the stacking sequence [18–22]. Heavy elements (Bi,Te,Pb) present in these compounds reduce the phonon group velocity and also the presence of many atoms in large unit cells lead to a large number of optical phonon modes. Presence of mixed cation layers causes strong phonon scattering which results in their

*These authors contributed equally to this work.
†asood@iisc.ac.in

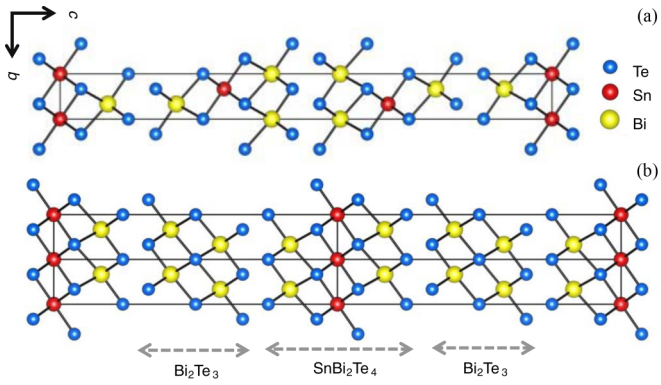

FIG. 1. (a) Crystal structure of $SnBi_2Te_4$ showing the 1.13- nm-thick seven atomic layers of $SnBi_2Te_4$. (b) Crystal structure of $SnBi_4Te_7$ showing a quintuple layer of Bi_2Te_3 and a septuple layer of $SnBi_2Te_4$. Red, Yyellow, and blue atoms represent Sn, Bi, and Te, respectively.

low thermal conductivity [23]. Thus, these compounds hold a lot of potential in the field of thermoelectrics owing to their low thermal conductivity as a result of several joint characteristics, such as, large unit cell with layered heterostructure causing strong phonon scattering. The majority members of this homologous series are also predicted to be 3D topological insulators [24–27].

Layered intergrowth compounds of the series $((SnTe)_m(Bi_2Te_3)_n)$, examples of natural van der Waals heterostructures, are layered compounds with dissimilar interlayer and intralayer interactions leading to intrinsic structural directionality. $SnBi_2Te_4$ [i.e., $(SnTe)(Bi_2Te_3)$] is a member of the $Sn_mBi_{2n}Te_{3n+m}$ homologous series with anisotropic layered tetradymite-type structure with $R\bar{3}m$ space group which can be viewed as the intergrowth of rocksalt SnTe (a TCI) and hexagonal (Bi_2Te_3) (a 3D TI) type phases. The crystal structure of $SnBi_2Te_4$ showing the 1.13-nm-thick seven atomic layers of $SnBi_2Te_4$ is shown in Fig. 1(a). The difference in the structure of $SnBi_2Te_4$ from that of the Bi_2Te_3 is that the central Te_2 layer of Bi_2Te_3 is replaced with a $Te_2 - Sn - Te_2$ trilayer in $SnBi_2Te_4$ [16]. The second layered compound of our interest of this homologous series is $SnBi_4Te_7$ [i.e., $(SnTe)_1(Bi_2Te_3)_2$] which crystallizes in trigonal structure with $P\bar{3}m1$ space group and can be viewed as a mixture of two units stacked along the c axis by van der Waals heterostructure, a quintuple layered Bi_2Te_3 and a septuple layered $SnBi_2Te_4$ [28] as shown in Fig. 1(b). These two compounds are predicted to be 3D TIs with metallic surface states, at ambient conditions [25].

Pressure dependent Raman study is a powerful tool to probe structural stability and phase transitions in materials by examining the change in pressure coefficients of phonon frequencies, and/or change in linewidth, and by the disappearance of existing modes or the appearance of new Raman modes. Recent high pressure resistivity measurements along with electronic band structure studies by Vilaplana *et al.* [27] have shown that $SnBi_2Te_4$ undergoes an electronic topological transition in the pressure regime of 3 to 5 GPa. Further, their x-ray diffraction study confirms another phase transition at ∼7 GPa, the exact nature of the transition still unknown [27]. Determination of high-pressure structures of these family of compounds have been challenging for a long time. A recent high-pressure x-ray diffraction study [29] on $MnBi_2Te_4$ and $MnBi_4Te_7$ shows pressure-induced amorphization of $MnBi_2Te_4$ at 17.4 GPa and two structural phase transitions in $MnBi_4Te_7$ at 14.4 and 18.6 GPa [29], respectively. On completion of our work, we became aware of a recent report by Li *et al.*, where they have observed pressure-induced superconductivity in $SnBi_2Te_4$ single crystals. Their high-pressure x-ray diffraction experiments on single crystals showed a structural transition from ambient trigonal structure to a monoclinic structure at 7.14 GPa and another structural transition to cubic structure above 18.9 GPa [30], and their observations are similar to the pressure-induced transitions observed in the parent compound Bi_2Te_3 [31].

In this work we have investigated the pressure dependent structural and vibrational properties of $SnBi_2Te_4$ and $SnBi_4Te_7$ using Raman and a combination of Raman and synchrotron x-ray diffraction measurements, respectively. Our studies indicate that at ∼6.0 GPa, rhombohedral ($R\bar{3}m$) $SnBi_2Te_4$ undergoes a structural transition to a possible monoclinic phase and an additional phase transition at ∼12 GPa associated with structural changes, similar to the observations reported by Li *et al.* [30]. We were tempted to compare our observations with the observations by Sans *et al.*, where they have reported a PID in ternary compound $SnSb_2Te_4$ [32], however the claim of PID could not be confirmed in the absence of detailed x-ray diffraction studies. $SnBi_4Te_7$ undergoes two structural phase transitions at ∼9.5 GPa and ∼14.1 GPa. Further, phonon anomalies in both the compounds indicate a low pressure transition (at 3–4 GPa) associated with a change in electronic topology, confirmed by our first-principles theoretical calculations. Our theoretical calculations indicate a band inversion occurring among valence and conduction bands of $SnBi_2Te_4$ and $SnBi_4Te_7$ in the Z-F and in Γ-M regions, respectively. In addition, using our Z_2 analysis in $SnBi_2Te_4$, we see a low pressure electronic topological transition (ETT), hitherto unreported, at a pressure (P_c) in between 0 GPa and 1 GPa, which is yet to be observed in experiments.

II. EXPERIMENTAL DETAILS

A general procedure was developed to synthesize the $SnBi_2Te_4$ and $SnBi_4Te_7$ heterostructured nanosheets by changing nominal composition of the precursors [anhydrous tin acetate, $Sn(OAc)_2$; bismuth neodecanoate and tri-n-octyl phosphine telluride (TOP-Te)] only. The details of the synthesis and characterization have been reported in Ref. [23]. High-pressure Raman studies were performed on both of these systems up to ∼17.0 GPa at room temperature using a Mao-Bell-type diamond anvil cell (DAC). The sample, along with a very small ruby chip (∼ 10 μm) were placed inside a hole of diameter ∼ 200 μm in a stainless steel gasket held between the two diamonds of the DAC. A methanol-ethanol-water (16:3:1 ratio) mixture was used as a pressure transmitting medium for both the cases. The ruby fluorescence method was used for pressure calibration [33]. For both the samples pressure dependent Raman spectra were recorded in LabRam spectrometer (M/s Horiba) in back-scattering geometry,

using 50X objective and laser excitation of 532 nm from a diode-pumped solid state laser. High-pressure synchrotron x-ray diffraction experiments were carried out on a powdered $SnBi_4Te_7$ sample at DESY PETRA (beam line P02.2) using a membrane-type diamond anvil cell up to ~25 GPa using a 0.2895 Å monochromatic x-ray radiation. The powdered $SnBi_4Te_7$ sample was loaded in a Rhenium gasket hole and neon was used as a pressure transmitting medium.

III. COMPUTATIONAL METHODS

Our first-principles calculations are based on density functional theory (DFT) employing the QUANTUM ESPRESSO [34] code. To treat the exchange and correlation energy of electrons, we used a generalized gradient approximation (GGA) [35] with a functional parametrized by Perdew, Burke, and Ernzerhof (PBE) [36]. The projector augmented wave (PAW) potentials [37] with valence configuration $4d^{10}\ 5s^2\ 5p^2$, $4d^{10}\ 5s^2\ 5p^4$ and $6s^2\ 6p^3\ 5d^{10}$ were adopted for Sn, Te, and Bi, respectively. Expansion of wave functions and charge density in plane wave basis set was truncated with energy cut-off of 50 and 400 Ry, respectively. The discontinuity in occupation numbers of the electronic states at the Fermi level was smeared with an energy width of $k_BT = 0.003$ Ry in the Fermi-Dirac distribution function. We include van der Waals interaction using PBE + D2 method of Grimme [38].

To study the pressure dependent phase transitions in $SnBi_2Te_4$, its rhombohedral $R\bar{3}m$ structure was theoretically analyzed. In calculations of $R\bar{3}m$ structure of $SnBi_2Te_4$, the Brillouin zone (BZ) integrations were sampled on a uniform mesh of 6×6×6 k points. High pressure structures of SnTe (*Pnma*) and Bi_2Te_3 ($C2/m$) were analyzed to examine the possibility of pressure induced decomposition of $SnBi_2Te_4$ at high pressures. BZ integrations were sampled on uniform 8x8x8 and 8x8x6 meshes of k points for SnTe (Pnma) and Bi_2Te_3 ($C2/m$) structures, respectively. To study pressure dependent phase transitions in $SnBi_4Te_7$, our analysis started with simulation of its low-pressure phase having trigonal structure with $P\bar{3}m1$ space group, and its BZ integrations were sampled on uniform 8x10x10 mesh of k points.

In simulations of pressure-dependent structural changes we used scalar-relativistic PAW potentials to optimize the structure with respect to lattice parameters and atomic coordinates, through minimization of enthalpy, H = E + PV at a given pressure. Effects of spin-orbit coupling (SOC) were included in our calculations of electronic structure through the use of fully relativistic [39] potentials. To assess electronic topology we have used Z2PACK code [40] to determine the Z_2 topological invariant and the mirror Chern number (n_M). This involves use of hybrid Wannier functions [41] and non-Abelian Berry phases [42], and the idea of time reversal polarization in calculations of the Z_2 invariants.

IV. RESULTS AND DISCUSSIONS

A. High-pressure studies on $SnBi_2Te_4$

1. Raman measurements

Raman spectra of $SnBi_2Te_4$ inside the DAC show four Raman modes (Fig. 2), marked as M2 (59.8 cm^{-1}), M3 (93.5 cm^{-1}), M4 (103.1 cm^{-1}) and M5 (136.5 cm^{-1}) at ambient pressure. The mode marked as M1 (29.7 cm^{-1}) starts to appear near 3.1 GPa because pressure induced shift in frequency brings it to the detectable range of our Raman set up. Three new modes marked as M7 (303.3 cm^{-1}), M8 (345.8 cm^{-1}) and M9 (489.7 cm^{-1}) appear above 6.0 GPa as shown in Figs. 2 and 3(a). As we increase the pressure, Raman spectra change significantly; the modes M3, M4, and M5 merge into a broad band and it becomes difficult to recognize the modes separately. A new mode marked as M6 (215.1 cm^{-1}) is seen at ~12 GPa. With increasing pressure the Raman modes become weaker in intensity and at 16.5 GPa, eight Raman modes are observed. Beyond 16.5 GPa, the modes become very broad and weak and hence could not be followed. Figure S1(a) (see Supplemental Material [43]) shows the Raman spectrum in the return pressure cycle. The broad band between 70 and 200 cm^{-1} does not change until the pressure value as low as 0.8 GPa. The starting four modes, M2, M3, M4, and M5 are seen to be present at 0 GPa with increased linewidths possibly due to high disorder. Thus, the pressure induced effects are not reversible and will be discussed later.

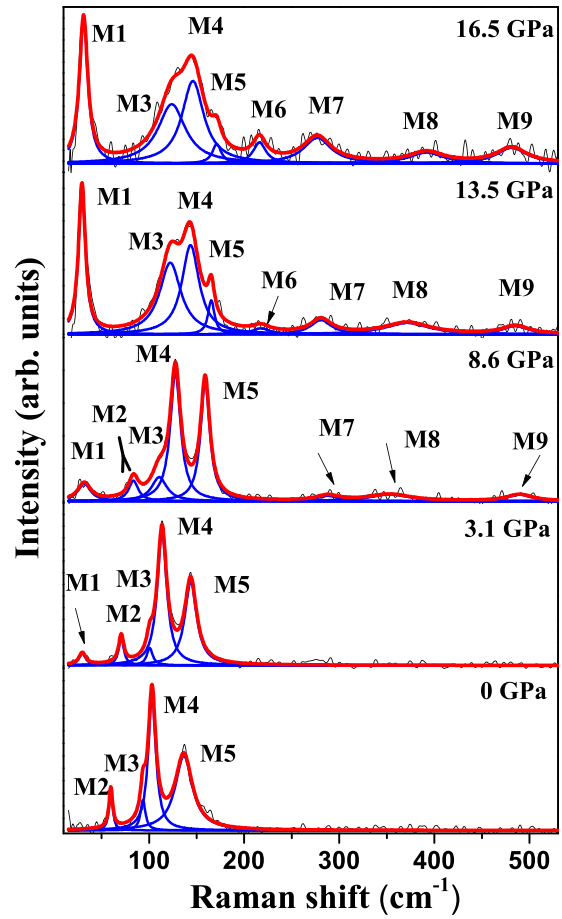

FIG. 2. Pressure evolution of Raman spectra of $SnBi_2Te_4$ in the increasing pressure run. Disappearance/appearance of new modes at different pressures are marked by arrows. Black solid lines are the experimental data. The solid red lines are Lorentzian fit to the experimental data. The blue solid lines are individual fits of the Raman modes.

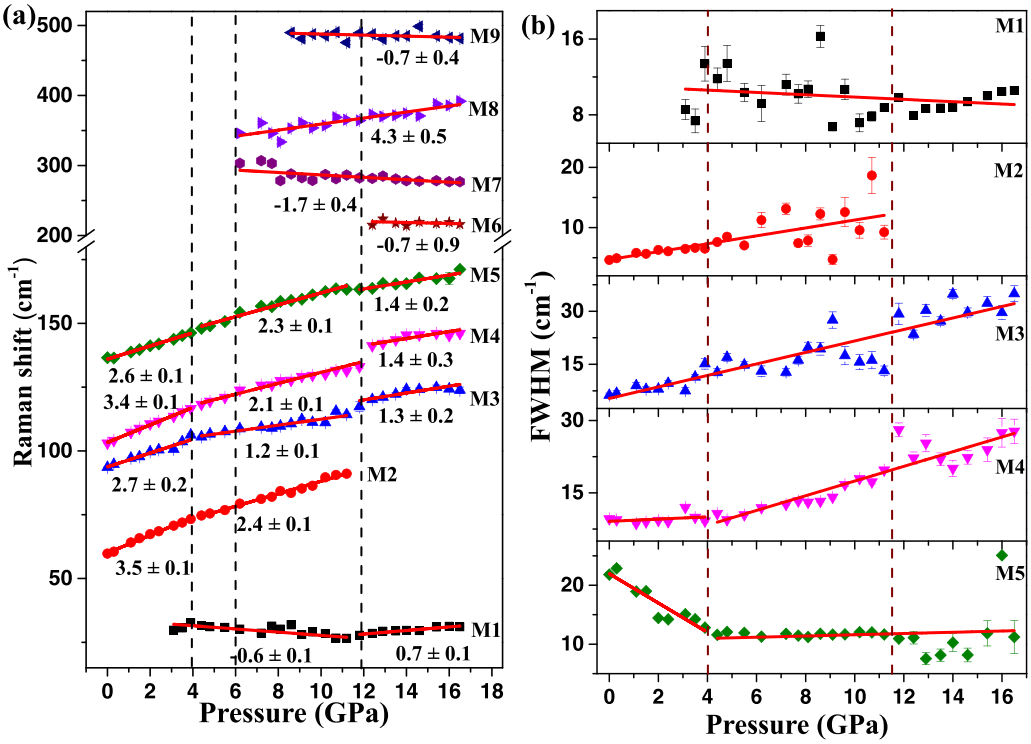

FIG. 3. (a) Raman shift of $SnBi_2Te_4$ is plotted against applied pressure for the increasing pressure run. The error bars are obtained from the fitting procedure. The solid red lines are the linear fits to the frequencies of the Raman modes in the increasing pressure run. The numbers depict the value of the slope $d\omega/d$P in cm^{-1} obtained from linear fits. The black dashed lines indicate the pressure where the transitions are taking place. (b) Pressure dependence of linewidth of the strong Raman modes of $SnBi_2Te_4$. The phase transition at ∼4.0 GPa is marked by the anomalous evolution of the full width at half maximum (FWHM) of the mode M5. The brown dashed lines indicate the pressure where the transitions are taking place. The solid red lines are the linear fits to the linewidths of the Raman modes in the two pressure regions below and above 4 GPa.

Figure 3(a) shows the pressure dependence of the frequency of the Raman modes which have been extracted from Lorentzian fits to the spectra at different pressures from the increasing pressure run. The solid lines are linear fits to the data of the increasing pressure run $\omega_P = \omega_0 + \frac{d\omega}{dP}P$. The values of the pressure coefficient, $d\omega/dP$, are mentioned on the graph. The following observations from Fig. 3(a) are noteworthy: (1) above 4 GPa, new Raman mode M1 is observed where M1 has a small negative pressure coefficient. (2) The pressure coefficients of the modes M2, M3, M4, and M5 change after 4 GPa. (3) Three new Raman modes M7, M8, and M9 are seen above 6.0 GPa. (4) Pressure coefficients of the modes M1, M3, M4, and M5 change at ∼12 GPa. (5) Mode M2 disappears above ∼12 GPa. (5) A new mode marked as M6 appears beyond ∼12 GPa. Figure 3(b) shows the variation of linewidths of the strong modes as a function of pressure which reveals that the linewidth of the mode M5 decreases till 4.0 GPa and then it does not vary much. Figure S1(b) (Supplemental Material [43]) shows pressure dependence of the frequency of the Raman modes for the decreasing pressure cycle which shows a considerable hysteresis in the pressure-induced changes. Figure S2 (Supplemental Material [43]) shows frequencies in the increasing and decreasing pressure runs on the same graph.

We recall that a low-pressure transition in the range of 3 to 5 GPa has been observed for the tetradymite TIs compound like Bi_2Te_3 [14,44], Bi_2Se_3 [45], Sb_2Te_3 [46] and Bi_2Te_2Se [47]. This transition is ETT in nature for Bi_2Te_3 [14,44],Sb_2Te_3 [46] and Bi_2Te_2Se [47] whereas it is only isostructural, without any change in electronic topology for Bi_2Se_3 [45]. High-pressure studies on $SnBi_2Te_4$ by Vilaplana *et al.* [27] report a minimum in the c/a ratio at ∼3.5 GPa, pointing to an isostructural transition, and the calculated electronic structure shows that the second valence band maxima crosses the Fermi level in the pressure range between 2 and 4 GPa, depending on the hole concentration. The Raman signature of phase transition at ∼6.0 GPa can be associated with a structural transition to the $C2/m$ phase (to be discussed later), as reported by Li *et al.* [30]. It can be observed from Figs. 2 and 3(a), that some of the Raman peaks merge to give a broad spectrum at ∼12 GPa, indicating a phase transition. Now, The $C2/m$ phase reported by Li *et al.* [30] is said to coexist with one or two other phases in the pressure range of 7.14–17.8 GPa and is reported to develop a cubic structure at pressures above 18.9 GPa. Thus, the Raman signature of phase transition observed in our Raman experiments at ∼12 GPa can be associated with a structural change, either due to coexistence of more than one phase with the $C2/m$ phase or a structural change to the cubic phase which takes place above 18.9 GPa as reported by Li *et al.* [30]. Additionally, the hysteresis in the pressure induced changes motivate us to look for a possibility of PID, which has been recently observed in the ternary compound $SnSb_2Te_4$ [32]. Our enthalpy calculations

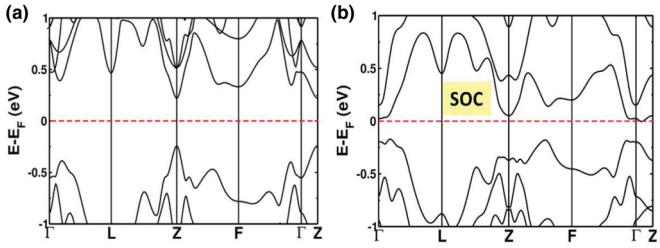

FIG. 4. Electronic structure of the low-pressure rhombohedral ($R\bar{3}m$) phase of $SnBi_2Te_4$ at P = 0 GPa calculated (a) without and (b) with the inclusion of effects of the spin orbit coupling at its optimized lattice parameter.

(to be presented later) suggests a possibility of $SnBi_2Te_4$ undergoing a PID into the parent binary compounds above ∼12 GPa. Keeping this in mind, we plot Raman shifts of $SnBi_2Te_4$ along with its parent compounds SnTe and Bi_2Te_3 against applied pressure (see Fig. S3 of the Supplemental Material [43]), which suggests a possibility of a partial PID, however, could not conclude PID. Thus, the nature of the phase transition observed in our Raman experiments at ∼12 GPa could not be confirmed without an x-ray diffraction study, and can be either due to structural changes (coexistence of different structural phases or a transition to the cubic phase) or can be associated with a partial PID (to be discussed later).

2. Theoretical Analysis

We now present theoretical analysis to understand pressure dependent transitions observed at P ∼4 GPa and ∼12 GPa. Our estimate of optimized lattice constant of rhombohedral ($R\bar{3}m$) phase of $SnBi_2Te_4$ in its primitive seven atoms unit cell is a = 14.32 Å, which is within the typical errors of GGA calculations relative to the experiment (a = 14.34 Å). Electronic structure of $SnBi_2Te_4$ calculated without spin-orbit interaction at the optimized lattice constant reveals a direct band gap of 0.51 eV at Z point [see Fig. 4(a)]. With SOC included [Fig. 4(b)], the conduction bands and valence bands are affected significantly, giving an indirect band gap of 0.195 eV. For further analysis SOC was included in our calculations of electronic structure. Besides, electronic structure up to hydrostatic pressure of 6 GPa was also calculated using scalar relativistic potentials (see Supplemental Material Fig. S4 [43]).

Upon compression, both the VBM (valence band maxima) and CBM (conduction band minimum) of $SnBi_2Te_4$ in the Z-F region gradually move towards the Fermi level with the energy gap reducing from 0.31 eV (0 GPa) to 0.10 eV (3 GPa) [Fig. 5(a)]. A close examination of electronic structure in the Z-F region [Figs. 5(a) and 5(b)] reveals a crossing of valence and conduction bands as the pressure increases from 3 to 4 GPa. At 3 GPa, isosurfaces of charge densities associated with VBM in the Z-F region reveal contributions from all Bi, Te, and Sn atoms, whereas dominant contributions from only Bi atoms are observed from iso-surfaces of charge densities associated with CBM in the Z-F region. However, at 4 GPa, VBM in the Z-F region has dominant contributions from only Bi atoms while CBM has contributions from all Bi,

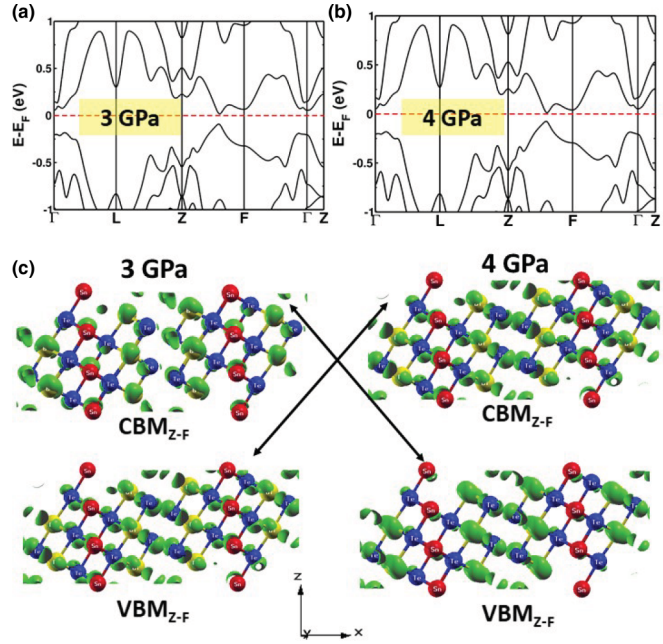

FIG. 5. Electronic structure of rhombohedral $SnBi_2Te_4$ at (a) P = 3 GPa and (b) 4 GPa. (c) Isosurfaces of charge densities associated with VBM and CBM in the Z-F region reveal inversion at the transition pressure. (Red, yellow, and blue atoms represent Sn, Bi, and Te, respectively).

Te, and Sn atoms. The inversion of states at VBM and CBM is thus evident from the isosurfaces of their charge densities [Fig. 5(c)]. Such band inversion is often an indicator of ETT in materials, and hence motivates us to determine the bulk electronic topology of $SnBi_2Te_4$. To quantify the change in topology due to band inversion, we determined the strong Z_2 topological index using a robust, quantitative and exact method as employed in the Z2PACK code [40]. The strong Z_2 topological invariant (ν_0) of $SnBi_2Te_4$ calculated at 3 GPa is $\nu_0 = 1$ (TI) which transforms to $\nu_0 = 0$ (normal insulator), at 4 GPa, thus confirming the change in electronic topology from topological insulator to the trivial band topology at pressures P > 3 GPa.

We calculated the topological invariant ν_0 at −1, 0, 1 and 2 GPa to be 0, 0, 1 and 1, respectively, predicting another low pressure ETT observed with transition pressure (P_c) in between 0 GPa and 1 GPa. Figure 6 summarizes our calculations. The change in Z_2 from 0 to 1 GPa arises from inversion of bands at the Γ point. The change in Z_2 under pressure dependent studies of $TlBiS_2$, and $TlSbS_2$ belonging to the same rhombohedral structure ($R\bar{3}m$) shows two isostructural ETTs [48,49]. Raman anomalies observed in $TlBiS_2$ at ∼0.5 and ∼1.8 GPa with corresponding first-principles DFT calculations have attributed these to topological phase transitions [48]. Since, $R\bar{3}\,m$ $SnBi_2Te_4$ can be viewed as the intergrowth of rocksalt SnTe (TCI) and hexagonal (Bi_2Te_3) (3D TI) type phases, the possibility of a nontrivial band topology with respect to crystalline symmetry (TCI phase) driven by the mirror symmetry of the hexagonal lattice needs to be examined as well. Hence, we calculated the mirror Chern number (n_M) as a function of pressure. Mirror symmetry in the crystal structure results in planes in the BZ that are mirror-

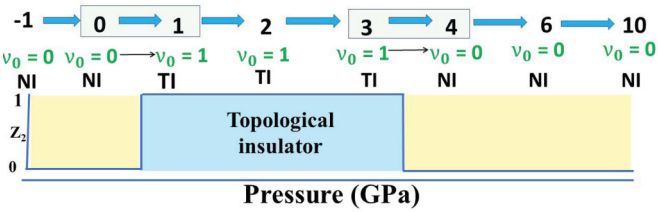

FIG. 6. ν_0 topological invariant of rhombohedral ($R\bar{3}m$) $SnBi_2Te_4$ calculated as a function of pressure ranging from −1 GPa to 10 GPa. NI and TI are normal insulator and topological insulator, respectively.

symmetric, leading to mirror symmetry protected Dirac cones in the surface electronic structure. A nonzero mirror Chern number 2 characterizes TCIs. The mirror Chern number defined as $n_M = (C_{+i} - C_{-i})/2$ can be used as a topological invariant for TCI, where C_{+i} and C_{-i} are the individual Chern numbers, defined on a mirror-invariant plane. The value of n_M upto 6 GPa is 1, confirming no change in electronic crystalline topology. In summary, pressure changes the topologically invariant Z_2 from $\nu_0 = 0$ (P = 0 GPa) to $\nu_0 = 1$ (P = 1 GPa) and at pressures higher than 3 GPa, the second band inversion results in $\nu_0 = 0$. The invariant quantities ν_0 and n_M at different pressures are summarized in Fig. 6.

Experimentally observed Raman modes of $SnBi_2Te_4$ above ∼6 GPa can be assigned to Raman modes of high-pressure $C2/m$ phase of $SnBi_2Te_4$, in agreement with a recent report by Li *et al.* However we want to stress here that Li *et al.* [30] show that the phase transition is sluggish and the $C2/m$ phase coexists with one or two of the other phases in pressure range of 7.14–17.8 GPa. Li *et al.* [30] show a monoclinic structure with the space group $C2/m$ was adopted using the full profile refinement via Le Bail fitting of the x-ray diffraction pattern of monoclinic phase coexisting with the initial phase. The lack of Rietveld refinement in any of the previous reports prevented us from obtaining the experimental atomic positions in $SnBi_2Te_4$ at high pressure, and therefore, we used the atomic positions of $C2/m$ phase of $YbFe_2O_4$ in our calculations to check for structural phase transition [50]. Nevertheless, all our attempts to theoretically identify the phase transition into a $C2/m$ high pressure (HP) phase failed. Previous HP studies [32] on similar compound $SnSb_2Te_4$ which also crystallizes in $R\bar{3}m$ phase at ambient conditions also failed to experimentally identify the structural phase transition to $C2/m$ phase. Motivated by Sans *et al.* [32] who showed experimental and theoretical evidence to establish PID of $SnSb_2Te_4$ and further provided theoretical evidence of PID in $SnBi_2Te_4$ we theoretically investigated the possibility of PID (see Fig. S5 of the Supplemental Material [43]). Our theoretical calculations suggest decomposition of $SnBi_2Te_4$ ($R\bar{3}m$) into orthorhombic SnTe (Pnma) and monoclinic Bi_2Te_3 ($C2/m$) at ∼11 GPa. However, the presence of PID can only be concluded by high-pressure x-ray diffraction (XRD) studies and hence we cannot conclude PID based only on our Raman results. To gain further insight into the 7 and 11 GPa transition, we examined the electronic properties of rhombohedral $SnBi_2Te_4$ up to hydrostatic pressure of 12 GPa. A detailed electronic structure along the full path and all

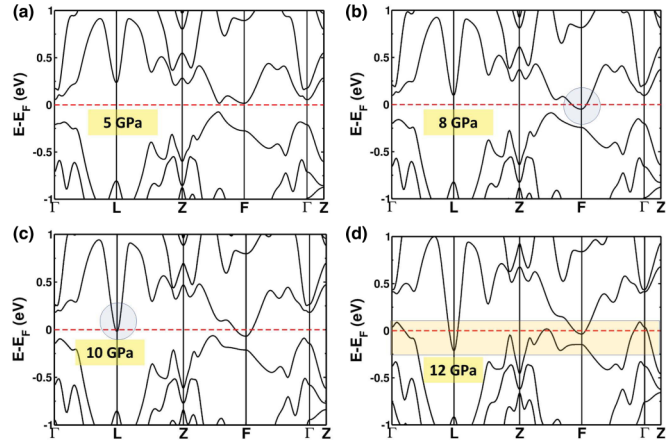

FIG. 7. Electronic structure of rhombohedral ($R\bar{3}m$) phase of $SnBi_2Te_4$ at (a) P = 5 GPa, (b) 8 GPa, (c) 10 GPa, and (d) 12 GPa calculated including the effects of spin-orbit coupling showing metallization at P ∼11GPa.

pressures are given in the Supplemental Material (see Fig. S6 of Ref. [43]). At 8 GPa [see Fig. 7(b)], electronic structure shows that the conduction band at the F point crosses the Fermi level. In addition, the CBM at the Z-point crosses the Fermi level at pressure of ∼10 GPa [see Fig. 7(c)]. At 12 GPa [see Fig. 7(d)] both the valence bands and conduction bands of $SnBi_2Te_4$ cross the Fermi level giving metallization of the $R\bar{3}m$ phase, through closure of the indirect band along the L-Z-F directions. The transition observed in experiments at ∼7 GPa is identified as a insulator to semimetal transition (occurring at 8 GPa). The electronic structure of high pressure $C2/m$ phase could not be examined due to the lack of Rietveld refinement in any of the previous reports.

B. High-pressure studies on $SnBi_4Te_7$

1. x-ray diffraction measurements

HP angular dispersive XRD measurements were performed on $SnBi_4Te_7$ in pressure steps of ∼1.5 GPa at room temperature. Figure 8(a) shows the collected XRD rings at 0.2 GPa. The bright ring near the center causes the intensity mismatch of the (014) (104) diffraction peaks from the ICSD reported data. The 2D diffraction images obtained at different pressures were integrated as a function of 2θ using the Dioptas software [51] to convert them into conventional one dimensional diffraction patterns. The Rietveld analysis of the XRD pattern at ambient pressure is performed using the FullProf software package [52] and is shown in Fig. 8(b). The 0.2-GPa diffraction peaks could be indexed to the trigonal crystal structure with space group $P\bar{3}m1$ (No. 164) by Rietveld refinement, in agreement with the reported results [53]. The obtained lattice parameters are a = 4.3942 Å, c = 24.0746 Å similar to [23,53] with $\chi^2 \sim 5.3$. The mismatch of the calculated pattern with the actual observed data generally observed in case of 2D nanosheets can be due to poor crystallinity.

The extracted lattice parameters (a and c) of the $Pm\bar{3}m$ phase of $SnBi_4Te_7$ are plotted in Fig. 9(a). The figure inset shows the variation of the c/a ratio as a function of pressure and it is observed to decreases rapidly till ∼4 GPa,

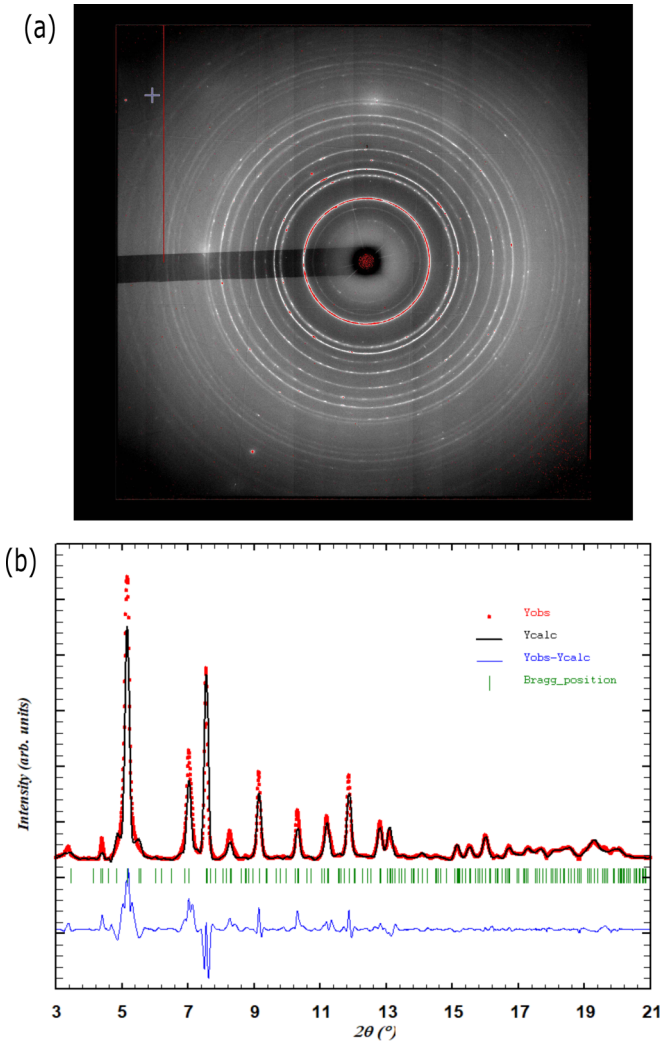

FIG. 8. (a) The image of Debye-Scherrer diffraction rings collected on the detector at ambient 0 GPa. The small red-polygons are drawn to mask the spots due to cosmic rays. (b) x-ray diffraction pattern of of $SnBi_4Te_7$ with the Rietveld refinement at 0.2 GPa.

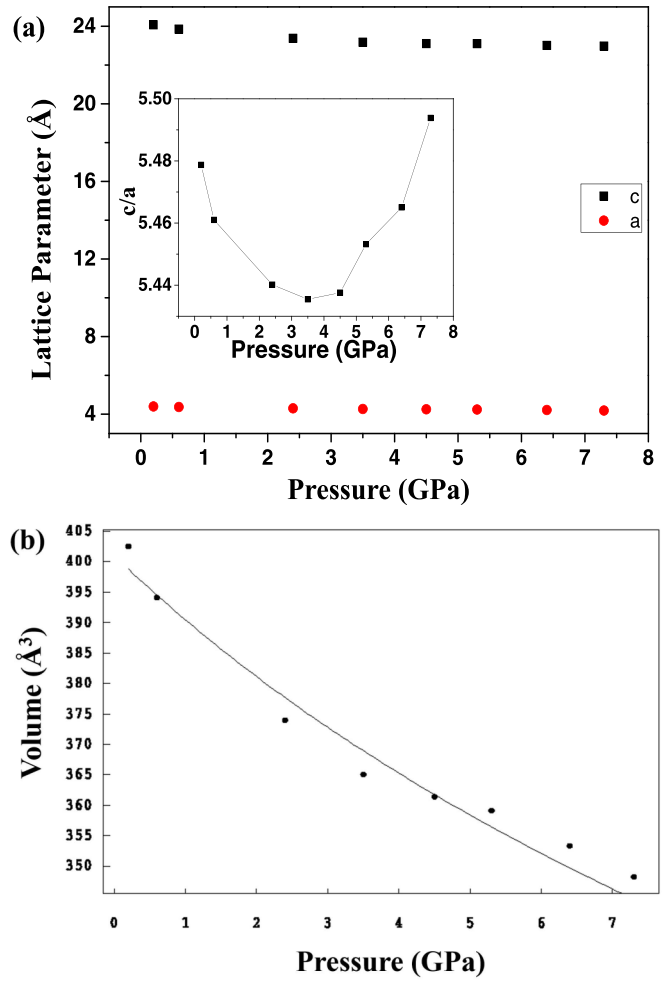

FIG. 9. (a) Pressure dependence of the lattice parameters of $SnBi_4Te_7$ under compression. The figure inset shows the pressure dependence of the axial c/a ratio. (b) Pressure dependence of the experimental volume of the ambient phase. The pressure-volume data is fitted using third-order Birch-Murnaghan equation.

implying that the c axis is more compressible than the a axis as expected from the anisotropy of layered crystals having weak van der Waals interlayer interactions along the c direction. Interestingly, the inflection point is noticed at ∼4 GPa, a similar trend in c/a ratio was previously reported in BiTeI [54], BiTeBr [55], and $TiTe_2$ [56], and these changes were interpreted as signatures of topological quantum phase transition. The changes in c/a ratio at ∼4 GPa are consistent with the ETT associated with band inversion of valence and conduction bands as a function of pressure near 4 GPa, to be discussed later. The pressure volume data is plotted in Fig. 9(b) with the third-order Birch-Murnaghan equation, using the EOSFIT7GUI software package [57]. From the fitting, the bulk modulus at the ambient pressure is $B_0 = 35.5$ GPa, with $B'_0 = 4.0$ GPa and the ambient pressure volume $V_0 = 401.0094$ Å^3. The obtained value of the bulk modulus is close to the reported value [27].

Figure 10 shows the evolution of the x-ray diffraction patterns as a function of pressure. In the low-pressure range of 0.2–7.3 GPa, phase I of $SnBi_4Te_7$ crystallizes in the trigonal $P\bar{3}m1$ space group and phase II, starts appearing at ∼9.1 GPa coexisting with phase I in the pressure range of 9.1–12.3 GPa. The diffraction pattern at ∼13.4 GPa is indexed to fully converted phase II. Phase III starts to appear at ∼14.3 GPa and phase II diminishes with increasing pressure. At the highest pressure of 25.1 GPa in our experiments, phase II is vanishingly small. Figure 11 shows a schematic representation of the presence of different phases as a function of pressure, as obtained from our x-ray diffraction study. For phase II of $SnBi_4Te_7$, Le Bail refinement using the WinPLOTR software [58] yielded a monoclinic structure with a = 15.0744 Å, b = 4.8317 Å, c = 14.9174 Å and $\beta = 149.5939°$. We suggest the space group of this monoclinic structure to be $C2/m$, similar to rhombohedral to monoclinic transition in Bi_2Te_3 [14,31,44], Bi_2Se_3 [44], Sb_2Te_3 [46] and Bi_2Te_2Se [47]. Following the high-pressure structural analysis of Bi_2Te_3 [31] and $MnBi_4Te_7$ [29] we assign phase III of $SnBi_4Te_7$ to be cubic $Im\bar{3}m$.

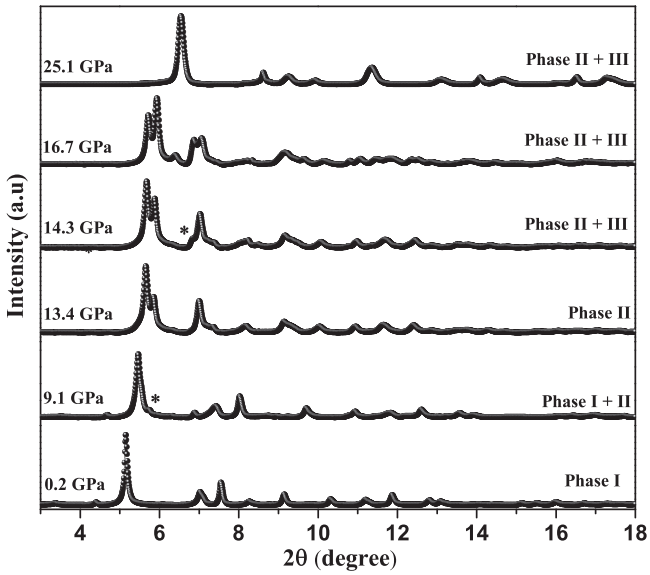

FIG. 10. X-ray diffraction patterns of $SnBi_4Te_7$ as a function of pressure. The new peaks appearing at 9.1 and 14.3 GPa are marked by star symbols. The changes in diffraction pattern at different pressures can be observed.

2. *Raman measurements*

Raman spectrum of $SnBi_4Te_7$ inside the DAC at P = 0 GPa shown in Fig. 12 displays Raman modes marked as M1 (34.5 cm^{-1}), M2 (59.9 cm^{-1}), M3 (93.5 cm^{-1}), M4 (102.8 cm^{-1}), M5 (135.6 cm^{-1}), M6 (213.1 cm^{-1}), M7 (275.5 cm^{-1}), and M8 (482.6 cm^{-1}). Above 14 GPa, the Raman spectrum completely changes and the modes marked by arrows merge into a broad band and it becomes difficult to identify the individual modes. With increasing pressure the Raman modes become weak in intensity similar to $SnBi_2Te_4$. As seen in Fig. 12, at the highest pressure of 17.0 GPa in our experiments, five Raman modes are observed. Beyond 17 GPa, the modes become very broad and the signal-to-noise ratio becomes low and hence we could not follow the modes. In return pressure cycle shown in Fig. S7(a) (see the Supplemental Material [43]) the broad nature of the Raman bands is present until 4.5 GPa. The eight modes observed are seen to recover at 2.4 GPa and the sample reverts to the starting phase at 0 GPa.

Figure 13(a) shows the pressure dependence of the frequency of the Raman modes for the increasing pressure run. The solid lines are linear fits with the values of the pressure derivative, $d\omega/dP$, marked on the graph. The following observations from Fig. 13(a) are noteworthy to mark the

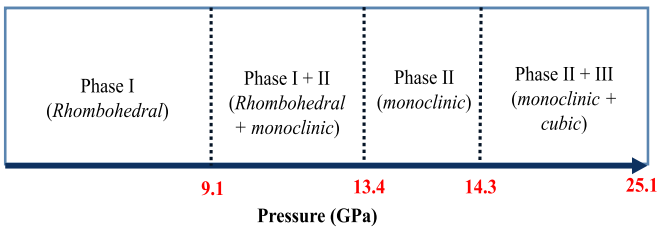

FIG. 11. Schematic representation of different phases of $SnBi_4Te_7$ as a function of pressure.

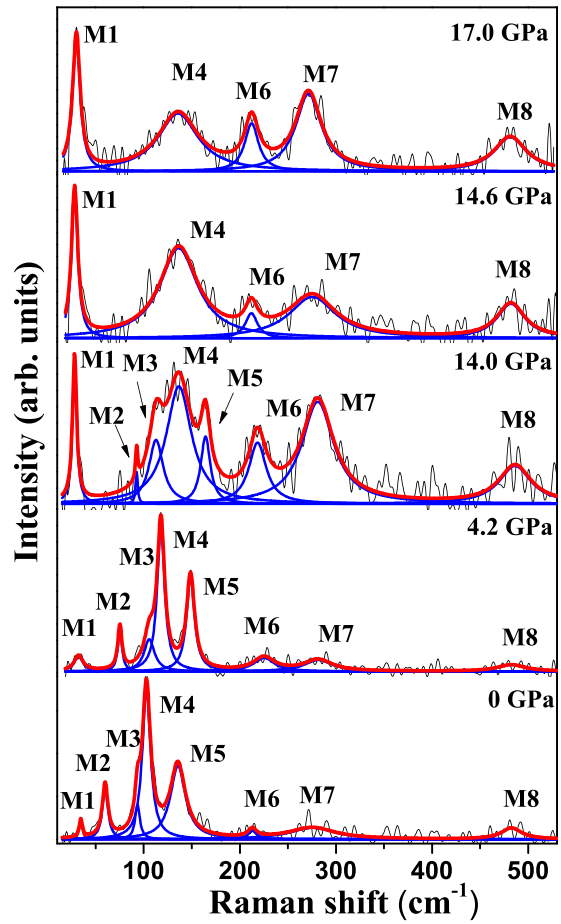

FIG. 12. Pressure evolution of Raman spectra of $SnBi_4Te_7$ in the increasing pressure run. Disappearance/appearance of new modes at different pressures are marked by arrows. Black solid lines are the experimental data. The solid red lines are Lorentzian fit to the experimental data. The blue solid lines are individual fits of the Raman modes.

phase transitions at 4, 9.5, and 14.1 GPa : (1) The pressure coefficients of the modes M1 to M5 change after 4 and at 9.5 GPa. (2) Modes M2, M3, and M5 are not observed beyond 14.0 GPa. The linewidths of the strong modes are shown in Fig. 13(b). The changes in the linewidths of M1, M3, and M5 around 4 GPa also mark the first transition. Figure S7(b) (Supplemental Material) shows pressure dependence of the frequency of the Raman modes for the decreasing pressure cycle indicating reversible nature of the sample as a function of pressure. Combining these observations with our x-ray data, the first transition at 4 GPa is isostructural whereas the second and third transitions are structural transitions to phase II (monoclinic) and phase III (cubic phase).

3. *Theoretical Analysis*

To understand the experimentally observed pressure anomalies in $SnBi_4Te_7$, we used first-principles calculations to simulate its trigonal $P\bar{3}m1$ phase as a function of pressure. Our theoretical estimates of lattice parameters of $P\bar{3}m1$ structure are a = b = 4.34 Å and c = 24.43 Å, respectively, which compare well with their experimental values

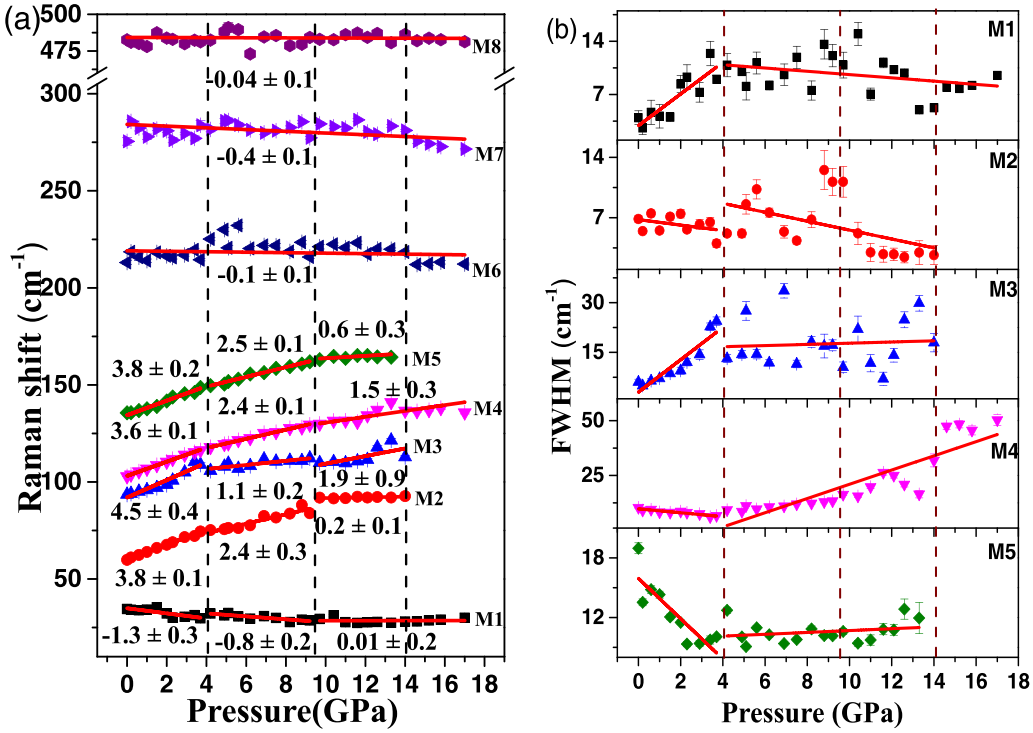

FIG. 13. Raman shift of $SnBi_4Te_7$ is plotted against applied pressure for the increasing pressure run. The error bars are obtained from the fitting procedure. The solid red lines are the linear fits to the frequencies of the Raman modes in the increasing pressure run. The numbers depict the value of the slope $d\omega/d$P in cm^{-1} obtained from linear fits. The black dashed lines indicate the pressure where the transitions are taking place. (b) Pressure dependence of linewidth of the strong Raman modes of $SnBi_4Te_7$. The phase transition at ∼4.0 GPa is marked by the anomalous evolution of the FWHM of the mode M5. The brown dashed lines indicate the pressure where the transitions are taking place. The solid red lines are the linear fits to the linewidths of the Raman modes in the two pressure regions below and above 4 GPa.

(a, b = 4.39 Å, c = 24.07 Å). At 0 GPa, its electronic structure (calculated without spin-orbit coupling) reveals well separated valence bands and conduction bands across the gap of 0.45 eV [Fig. 14(a)]. Inclusion of SOC results in significant changes both in conduction bands and valence bands, reducing the bandgap to 0.20 eV [see Fig. 14(b)]. Besides, the importance of SOC for this class of materials was systematically studied and analyzed in our calculations by performing electronic structure calculations using scalar relativistic potentials as well (see Supplemental Material Fig. S8 of Ref. [43]). Under compression, both the VBM and the CBM gradually move towards the Fermi level, and electronic energy band gap reduces from 0.2 eV at 0 GPa to 0.08 eV at 3 GPa [Fig. 15(d)].

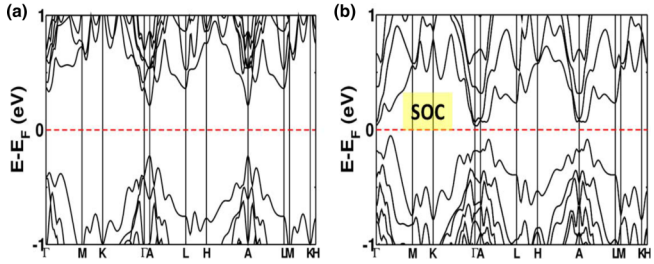

FIG. 14. Electronic structure of the low-pressure trigonal ($P\bar{3}m1$) structure of $SnBi_4Te_7$ at P = 0 GPa calculated (a) without and (b) with the inclusion of effects of the spin orbit coupling at its optimised lattice parameter.

With further increase in pressure from 3 to 8 GPa, the energy gap in the Γ-M region monotonically increases and reaches 0.12 eV at 8 GPa. A detailed electronic structure along the full path and all pressures are given in the Supplemental Material (see Fig. S9, Ref. [43]). In the Γ-M region, band inversion occurs at P between 3 and 4 GPa, as is evident in

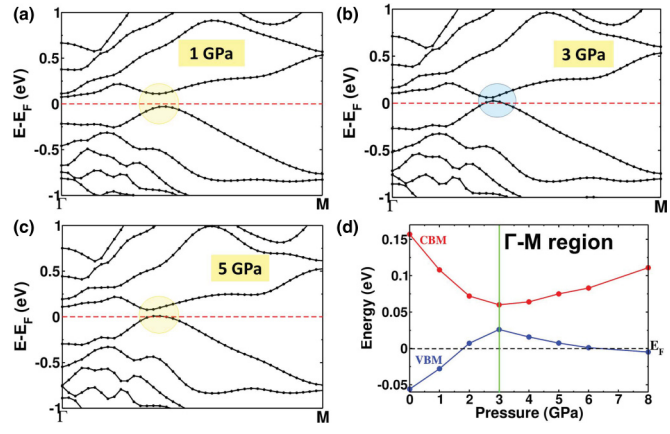

FIG. 15. Electronic structure of trigonal ($P\bar{3}m1$) structure of $SnBi_4Te_7$ calculated with spin-orbit coupling at (a) 1 GPa, (b) 3 GPa and (c) 5 GPa and (d) variation in VBM and CBM with pressure in Γ-M region of the Brillouin zone showing the opening and closing of gap at the critical pressure ∼3 GPa.

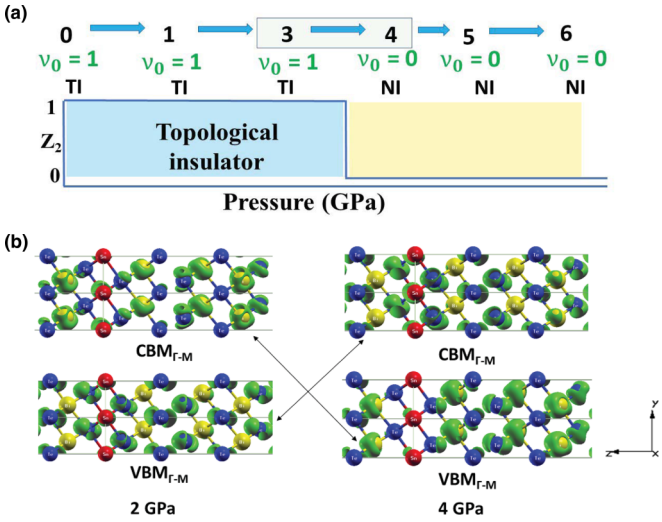

FIG. 16. (a) ν_0 topological invariant of trigonal ($P\bar{3}m1$) $SnBi_4Te_7$ evaluated as a function of pressure ranging from 0 GPa to 6 GPa. NI and TI are normal insulator and topological insulator respectively. (b) Isosurface of charge densities associated with VBM and CBM in the Γ-M region reveal inversion at the critical pressure P ∼3 GPa. (Red, yellow, and blue atoms represent Sn, Bi, and Te, respectively).

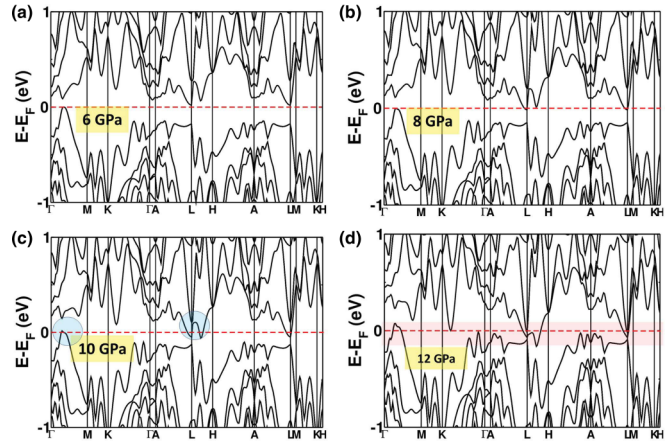

FIG. 17. (a) Electronic structure of the trigonal ($P\bar{3}m1$) structure of $SnBi_4Te_7$ at (a) P = 6 GPa, (b) 8 GPa, (c) 10 GPa, and (d) 12 GPa calculated with the inclusion of effects of the spin-orbit coupling showing a insulating to semimetallic transition with increasing pressure resulting from valence band maxima (VBM) and conduction band minima (CBM) crossing Fermi level at P = 10 GPa.

the isosurfaces of charge densities [see Fig. 16(b)] of states at VBM and CBM at 2 and 4 GPa.

To verify the change in topology upon band inversion, we determined the strong Z_2 topological index employed in the Z2PACK code [40]. The strong Z_2 topological invariant (ν_0) of $SnBi_4Te_7$ is $\nu_0 = 1$ (TI) at 3 GPa and $\nu_0 = 0$ (normal insulator) at 4 and 5 GPa, confirming the change in electronic topology and establishing the first phase transition to be a topological phase transition [Fig. 16(a)]. The mirror Chern number used as a topological invariant for TCI was not evaluated for $SnBi_4Te_7$. To probe the experimentally observed transition at 9.5 GPa, we carefully examined band structure of the $P\bar{3}m1$ phase of $SnBi_4Te_7$. With increasing hydrostatic pressure, evolution of electronic structure reveals emergence of semimetallic behavior of $P\bar{3}m1$ phase, with valence band (VB) and conduction band (CB) crossing the Fermi level at 10 GPa [Fig. 17(c)]. Thus, with increasing hydrostatic pressure (from 0 GPa to 10 GPa), the $P\bar{3}m1$ phase undergoes an insulator to semimetal phase transition followed by complete metallization of at P = 12 GPa. The transition observed in our experiments at ∼9.5 GPa is thus identified as an insulator to semimetal transition.

V. CONCLUSIONS

In summary, high-pressure Raman experiments on $SnBi_2Te_4$ and $SnBi_4Te_7$ have revealed that both the compounds undergo an isostructural transition in the pressure regime of 3 to 5 GPa. Our first-principles theoretical analysis shows that the low pressure (3 GPa) Raman anomalies in $SnBi_2Te_4$ are associated with inversion of the valence and conduction bands in Z-F region in the BZ, resulting in change in the electronic topology of $SnBi_2Te_4$. The 3 GPa transition in $SnBi_4Te_7$ is an ETT associated with band inversion of valence and conduction bands in Γ-M region as a function of pressure. Our experiments show $SnBi_2Te_4$ undergoes structural transition at ∼6 and ∼12 GPa into a possible monoclinic phase and a cubic phase, respectively. In addition, this transition involves a semimetal to metal transition shown through our calculation of electronic structure. On the other hand, $SnBi_4Te_7$ undergoes two structural transitions, at ∼9.5 and ∼13.8 GPa. The transition at ∼9.5 GPa is associated with a structural transition from trigonal phase I to a mixed phase (phase I + phase II), where phase II has a monoclinic structure. The second phase transition at ∼13.8 GPa is associated with transition to cubic Phase III. Subsequently, phases II and III coexist beyond 13.8 GPa. Our theoretical analysis shows that the experimentally observed Raman anomalies in $SnBi_4Te_7$ at 9.5 GPa are possibly associated with an insulator to semimetal transition. We hope that our results showing the effect of pressure on electronic and crystal structure of the two compounds will motivate further experimental and theoretical studies on these family of layered natural van der Waals heterostructures for better understanding of their tuning of topological properties as a function of pressure.

ACKNOWLEDGMENTS

A.K.S. acknowledges funding from the Department of Science and Technology (DST), India under Year of Science Professorship and the Nanomission Council. S.P. acknowledges DST for Inspire fellowship. The authors gratefully acknowledge the financial support by Jawaharlal Nehru Center for Advanced Scientific Research (JNCASR) from the DST-DESY project to carry out the high-pressure synchrotron XRD measurements at the P02.2 beam line, Petra-III, DESY, Germany. S.P. also acknowledges K. Mallick and S. Pittala for their help in XRD data analysis. R.A. thanks JNCASR for the research fellowship. U.V.W. acknowledges support from a J.C Bose National Fellowship. K.B. acknowledges the Swarnajayanti fellowship, DST.

[1] M. Z. Hasan and C. L. Kane, Rev. Mod. Phys. **82**, 3045 (2010).
[2] X.-L. Qi and S.-C. Zhang, Rev. Mod. Phys. **83**, 1057 (2011).
[3] P. Roushan, J. Seo, C. V. Parker, Y. S. Hor, D. Hsieh, D. Qian, A. Richardella, M. Z. Hasan, R. J. Cava, and A. Yazdani, Nature (London) **460**, 1106 (2009).
[4] J. Seo, P. Roushan, H. Beidenkopf, Y. S. Hor, R. J. Cava, and A. Yazdani, Nature (London) **466**, 343 (2010).
[5] Y. L. Chen, J. G. Analytis, J.-H. Chu, Z. K. Liu, S.-K. Mo, X. L. Qi, H. J. Zhang, D. H. Lu, X. Dai, Z. Fang, S. C. Zhang, I. R. Fisher, Z. Hussain, and Z.-X. Shen, Science **325**, 178 (2009).
[6] H. Zhang, C.-X. Liu, X.-L. Qi, X. Di, Z. Fang, and S.-C. Zhang, Nat. Phys. **5**, 438 (2009).
[7] T. H. Hsieh, H. Lin, J. Liu, W. Duan, A. Bansil, and L. Fu, Nat. Commun. **3**, 982 (2012).
[8] J. C. Y. Teo, L. Fu, and C. L. Kane, Phys. Rev. B **78**, 045426 (2008).
[9] L. Fu, Phys. Rev. Lett. **106**, 106802 (2011).
[10] Y. Tanaka, Z. Ren, T. Sato, K. Nakayama, S. Souma, T. Takahashi, K. Segawa, and Y. Ando, Nat. Phys. **8**, 800 (2012).
[11] J. Liu, W. Duan, and L. Fu, Phys. Rev. B **88**, 241303(R) (2013).
[12] S. Pal, R. Arora, S. ROychowdhury, L. Harnagea, K. Saurabh, S. Shenoy, D. V. S. Muthu, K. Biswas, U. V. Waghmare, and A. K. Sood, Phys. Rev. B **101**, 155202 (2020).
[13] A. Polian, M. Gauthier, S. M. Souza, D. M. Trichês, J. C. de Lima, T. A. Grandi, Phys. Rev. B **83**, 113106 (2011).
[14] G. K. Pradhan, A. Bera, P. Kumar, D. V. S. Muthu, and A. K. Sood, Solid State Commun. **152**, 284 (2012).
[15] L. E. Shelimova, O. G. Karpinskii, P. P. Konstantinov, E. S. Avilov, M. A. Kretova, and V. S. Zemskov, Inorg. Mater. **40**, 451 (2004).
[16] O. G. Karpinskii, L. E. Shelimova, M. A. Kretova, E. S. Avilov, and V. S. Zemskov, Inorg. Mater. **39**, 240 (2003).
[17] A. Chatterjee and K. Biswas, Angew. Chem. Int. Ed. **54**, 5623 (2015).
[18] S. V. Eremeev, Y. M. Koroteev, and E. V. Chulkov, JETP Lett. **92**, 161 (2010).
[19] S. V. Eremeev, G. Landolt, T. V. Menshchikova, B. Slomski, Y. M. Koroteev, Z. S. Aliev, M. B. Babanly, J. Henk, A. Ernst, L. Pattheya, A. Eich, A. A. Khajetoorians, J. Hagemeister, O. Pietzsch, J. Wiebe, R. Wiesendanger, P. M. Echenique, S. S. Tsirkin, I. R. Amiraslanov, J. H. Dil *et al.*, Nat. Commun. **3**, 635 (2012).
[20] M. G. Vergniory, T. V. Menshchikova, S. V. Eremeev, and E. V. Chulkov, Appl. Surf. Sci. **267**, 146 (2013).
[21] K. Kuroda, H. Miyahara, M. Ye, S. V. Eremeev, Yu. M. Koroteev, E. E. Krasovskii, E. V. Chulkov, S. Hiramoto, C. Moriyoshi, Y. Kuroiwa, K. Miyamoto, T. Okuda, M. Arita, K. Shimada, H. Namatame, M. Taniguchi, Y. Ueda, and A. Kimura, Phys. Rev. Lett. **108**, 206803 (2012).
[22] K. Okamoto, K. Kuroda, H. Miyahara, K. Miyamoto, T. Okuda, Z. S. Aliev, M. B. Babanly, I. R. Amiraslanov, K. Shimada, H. Namatame, M. Taniguchi, D. A. Samorokov, T. V. Menshchikova, E. V. Chulkov, and A. Kimura, Phys. Rev. B **86**, 195304 (2012).
[23] A. Banik and K. Biswas, Angew. Chem. **129**, 14753 (2017).
[24] K. Nakayama, K. Eto, Y. Tanaka, T. Sato, S. Souma, T. Takahashi, K. Segawa, and Y. Ando, Phys. Rev. Lett. **109**, 236804 (2012).
[25] K. Yang, W. Setyawan, S. Wang, M. B. Nardelli, and S. Curtarolo, Nat. Mater. **11**, 614 (2012).
[26] M. G. Vergniory, T. V. Menshchikova, I. V. Silkin, Y. M. Koroteev, S. V. Eremeev, and E. V. Chulkov, Phys. Rev. B **92**, 045134 (2015).
[27] R. Vilaplana, J. A. Sans, F. J. Manjón, A. Andrada-Chacón, J. Sánchez-Benítez, C. Popescu, O. Gomis, A. L. J. Pereira, B. GarcíaDomene, P. Rodríguez-Hernández, A. Muñoz, D. Daisenberger, and O. Oeckler, J. Alloys Compd. **685**, 962 (2016).
[28] A. K. Geim and I. V. Grigorieva, Nature (London) **499**, 419 (2013).
[29] C. Pei, Y. Xia, J. Wu, Y. Zhao, L. Gao, T. Ying, B. Gao, N. Li, W. Yang, D. Zhang, H. Gou, Y. Chen, H. Hosono, G. Li, and Y. Qi, Chin. Phys. Lett. **37**, 066401 (2020).
[30] R. Li, G. Liu, Q. Jing, X. Wang, H. Wang, J. Zhang, and Y. Ma, J. Alloys Compd. **900**, 163371 (2022).
[31] L. Zhu, H. Wang, Y. Wang, J. Lv, Y. Ma, Q. Cui, Y. Ma, and G. Zou, Phys. Rev. Lett. **106**, 145501 (2011).
[32] J. A. Sans, R. Vilaplana, E. L.- da Silva, C. Popescu, V. P. Cuenca-Gotor, A. Andrada-Chacón, J. Sańchez-Benitez, O. Gomis, A. J. Pereira, P. Rodríguez-Hernandez, A. Munòz, D. Daisenberger, B. García-Domene, A. Segura, D. Errandonea, R. S. Kumar, O. Oeckler, P. Urban, J. Contreras-García, and F. J. Manjon, Inorg. Chem. **59**, 9900 (2020).
[33] H. K. Mao, J. Xu, and P. M. Bell, J. Geophys. Res. **91**, 4673 (1986).
[34] QUANTUM-ESPRESSO is a community project for high-quality quantum-simulation software, based on density-functional theory, and coordinated by P. Giannozzi. See http://www.quantum-espresso.org and http://www.pwscf.org.
[35] X. Hua, X. Chen, and W. A. Goddard III, Phys. Rev. B **55**, 16103 (1997).
[36] J. P. Perdew, K. Burke, and M. Ernzerhof, Phys. Rev. Lett. **77**, 3865 (1996).
[37] G. Kresse and D. Joubert, Phys. Rev. B **59**, 1758 (1999).
[38] S. Grimme, J. Comput. Chem. **25**, 1463 (2004).
[39] A. Dal Corso, Comput. Mater. Sci. **95**, 337 (2014).
[40] D. Gresch, G. Autès, O. V. Yazyev, M. Troyer, D. Vanderbilt, B. A. Bernevig, and A. A. Soluyanov, Phys. Rev. B **95**, 075146 (2017).
[41] A. A. Soluyanov and D. Vanderbilt, Phys. Rev. B **83**, 235401 (2011).
[42] J. Bhattacharjee and U. V. Waghmare, Phys. Rev. B **71**, 045106 (2005).
[43] See Supplemental Material at http://link.aps.org/supplemental/10.1103/PhysRevB.106.134104 for additional experimental and theoretical results.
[44] R. Vilaplana, O. Gomis, F. J. Manjón, A. Segura, E. Pérez-González, P. Rodríguez-Hernández, A. Muñoz, J. González, V. Marín-Borrás, V. Muñoz-Sanjosé, C. Drasar, and V. Kucek, Phys. Rev. B **84**, 104112 (2011).
[45] A. Bera, K. Pal, D. V. S. Muthu, U. V. Waghmare, and A. K. Sood, J. Phys.: Condens. Matter **28**, 105401 (2016).
[46] O. Gomis, R. Vilaplana, F. J. Manjón, P. Rodríguez-Hernández, E. Pérez-González, A. Muñoz, V. Kucek, and C. Drasar, Phys. Rev. B **84**, 174305 (2011).
[47] M. B. Nielsen, P. Parisiades, S. R. Madsen, and M. Bremholm, Dalton Trans. **44**, 14077 (2015).

[48] V. Rajaji, R. Arora, S. C. Sarma, B. Joseph, S. C. Peter, U. V. Waghmare, and C. Narayana, Phys. Rev. B **99**, 184109 (2019).
[49] Q. Zhang, Y. Cheng, and U. Schwingenschlöl, Sci. Rep. **5**, 8379 (2015).
[50] K. Fujiwara, Y. Fukada, Y. Okuda, R. Seimiya, N. Ikeda, K. Yokoyama, H. Yu, S. Koshihara, and Y. Okimoto, Sci. Rep. **11**, 4277 (2021).
[51] C. Prescher and V. B. Prakapenka, High Press. Res. **35**, 223 (2015).
[52] https://www.ill.eu/sites/fullprof/.
[53] B. A. Kuropatwa and H. Kleinke, Z. Anorg. Allg. Chem. **638**, 2640 (2012).
[54] V. Rajaji, U. Dutta, P. C. Sreeparvathy, S. C. Sarma, Y. A. Sorb, B. Joseph, S. Sahoo, S. C. Peter, V. Kanchana, and C. Narayana, Phys. Rev. B **97**, 085107 (2018).
[55] X. Xi, C. Ma, Z. Liu, Z. Chen, W. Ku, H. Berger, C. Martin, D. B. Tanner, and G. L. Carr, Phys. Rev. Lett. **111**, 155701 (2013).
[56] A. Ohmura, Y. Higuchi, T. Ochiai, M. Kanou, F. Ishikawa, S. Nakano, A. Nakayama, Y. Yamada, and T. Sasagawa, Phys. Rev. B **95**, 125203 (2017).
[57] R. J. Angel, J. Gonzalez-Platas, and M. Alvaro, Z. Kristallogr. **229**, 405 (2014).
[58] https://www.cdifx.univ-rennes1.fr/winplotr/winplotr.htm.